Experimental investigation of the process of corrosion-caused cover cracking

Yanlong Zhang and Ray Kai Leung Su[1]

Department of Civil Engineering, The University of Hong Kong, Pokfulam Road, Hong Kong, PRC

Abstract: Corrosion-caused cover cracking can lead to the serious deterioration of reinforced concrete (RC) structures. However, only a few experimental studies in the literature have examined the entire cracking process of specimens with a realistic configuration that consists of both the concrete cover and concrete core. Herein, the mechanism and process of cover cracking are experimentally investigated for cover and core specimens by using accelerated corrosion tests together with digital image correlation. The entire process of corrosion-caused cover cracking is experimentally recorded. The phenomenon of the rotation of the cover is first observed. Furthermore, the direction of the crack propagation, crack opening displacement (COD) profiles and the concrete expansion at the steel/concrete interface are measured. The relationship between total rust and the rust that causes expansion pressure on the surrounding concrete is examined. The test results are then used to validate a previously proposed elastic-body-rotation model for simulating cover cracking.

Keywords: Corrosion; Cover cracking; DIC; Experimental study; COD; Rust

1. Introduction

The expansion caused by the corrosion of rebars, shrinkage, thermal stress, external loading, etc. can cause the cracking of reinforced concrete (RC) structures. In particular, the corrosion of rebars has been widely considered as one of the most predominant deterioration processes [1-3] due to the fact that corrosion-caused cover cracking can reduce the strength of the concrete cover and degrade the bonding strength between the rebar and concrete as well as cause water leakage. These can adversely affect the serviceability, strength, durability, and ductility of RC structures [4-16]. However, the challenge lies in fully understanding the deterioration mechanisms as the phenomena of crack initiation, propagation and widening that take place in concrete cannot be readily observed.

In the literature, two typical specimen configurations are used to study the deterioration of the concrete cover caused by the corrosion of one of the inner rebars; see Fig. 1. In the figure, c denotes the thickness of the concrete cover and D is the diameter of the rebar. Fig. 1a illustrates the concrete cover specimen. These specimens have a single rebar placed at the center of a concrete cylinder or a concrete cube and the thickness of the concrete around the rebar is equal to the simulated cover thickness.

1 Corresponding author. Tel.:+852 2859 2648
E-mail address: klsu@hku.hk (RKL Su)

Fig. 1b shows a cover and core specimen that features different concrete thicknesses around the rebar in which the thinner side represents the concrete cover and the thicker side simulates the concrete core.

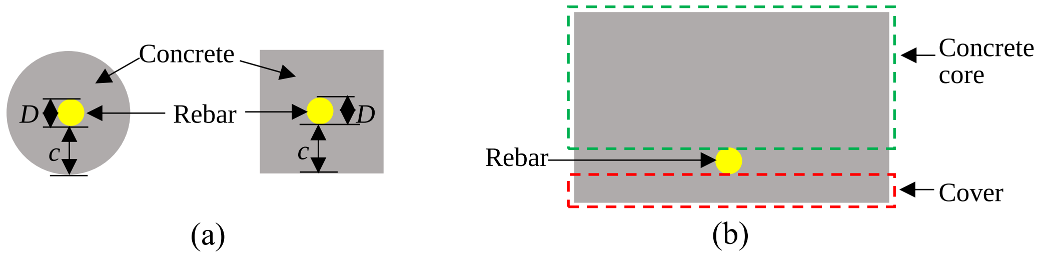

Fig. 1 Two typical configurations for studying deterioration of concrete cover caused by corroded inner rebar (a) concrete cover specimen, and (b) cover and core specimen

The induced crack patterns in the cover and cover and core specimens as shown in Fig.2 are different due to the different distributions of rust around the rebar and different confinement pressure from the concrete. Most real RC members consist of a cover and a concrete core. The confinement effects in the lateral direction of the cover and core specimen are greater than those in the direction normal to the cover surface. The cover and core specimens which can be used to realistically model the confinement effects are more suitable for studying cracking of the concrete cover caused by a corroded rebar. Furthermore, aggressive ions, like chloride or sulfate ions, usually penetrate through the thinner cover surface and first reach the rebar surface that is in proximity to the concrete cover which causes the depassivation of this part of the rebar first in typical RC members in aggressive environments [17-20]. As a result, there is the initiation of macrocell corrosion between the corroded and non-corroded rebars, which results in more rust near the cover than the concrete core [21-25]. Thus the cover and core specimens can more realistically simulate the rust distribution around corroded rebars.

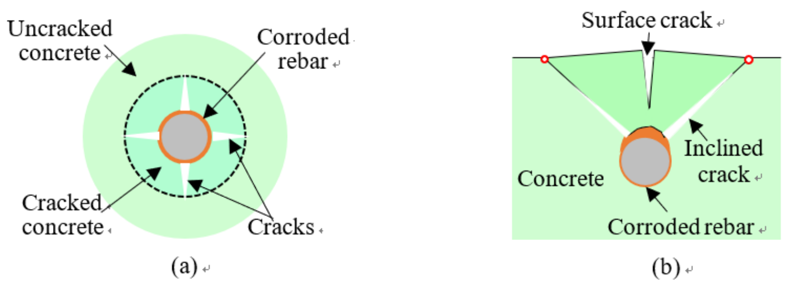

Fig. 2 Cracked cover in (a) cover specimen vs. (b) cover and core specimen

The differences in cracking process and deformation between the cover specimens and cover and core specimens are summarized here.

1. In the cover specimens, corrosion-caused cracks initiate at the steel/concrete interface and then propagate toward the cover surface (from inside to outside)

[26-30], while in the cover and core specimens, surface crack always initiates at the cover surface and then spreads toward the rebar (from outside to inside) [17, 31-34].

2. The COD profile of the surface crack decreases from the steel/concrete interface to the cover surface in the cover specimens [28, 35], whereas an opposite COD profile is found in the cover and core specimens [32, 33, 36].
3. The expansion of rust causes tangential tension in concrete and uniform expansion of concrete around the rebar in the cover specimens [29, 37, 38]. However, the expansive force of the rust pushes against the concrete cover and causes its rotation. As a result, there is a much larger movements of the cover than the core in the cover and core specimens [36].

Experimentally and numerically studies [11, 17, 32, 33, 39-41] have been conducted to investigate corrosion caused cracking of cover and core. However, only the width of surface cracks at the end of the test were presented in the experimental studies [11, 39, 41]. The changes in crack patterns and COD profiles throughout the test were not reported. Even though the cracking process was numerically and analytically simulated [17, 32, 33], their predicted results have not been validated experimentally. It is therefore imperative to conduct related experimental test and display the entire process of cover deterioration caused by rebar corrosion for comparison.

Digital image correlation (DIC) is an optical-based technique for measuring surface displacement. The basic principle of this technique is to search for the maximum correlation between small zones in two images of a specimen. In calculating the displacement, one small zone from the first image is defined as the reference, and the corresponding zone on the other image is defined as the target. The displacements at various points in the reference zone can be obtained by calculating the differences in the coordinates of the speckle pattern in the two zones [42, 43]. This technique is both a non-contact and non-destructive means for measuring the surface deformation of a specimen subjected to external forces. One of the main advantages of this method is that the entire cracking process, including crack initiation, propagation and widening, can be continuously measured. The DIC method has been widely used in measuring the cracking of RC structures [44-49].

In this study, the mechanism and process of concrete cover cracking are experimentally investigated by using accelerated corrosion tests together with DIC. The corrosion-caused cover rotation, bulging of the cover surface, displacement at the steel/concrete interface and COD profiles are recorded. The concrete strain around the rebar is also measured by using strain gauges. Furthermore, the relationship between the total rust and the rust that causes expansion pressure on the surrounding concrete is evaluated.

2. Analytical model

An elastic-body-rotation model was proposed by [36] to analyze the mechanism and process of cover cracking caused by the corrosion of an inner rebar. This model can be used to estimate the volume of corroded steel that would cause the initiation of cracking. Furthermore, a relationship was found between the surface crack width and the volume of corroded steel in [36]. Therefore, the experimental results obtained from [36] will be used to validate the proposed analytical model in this study.

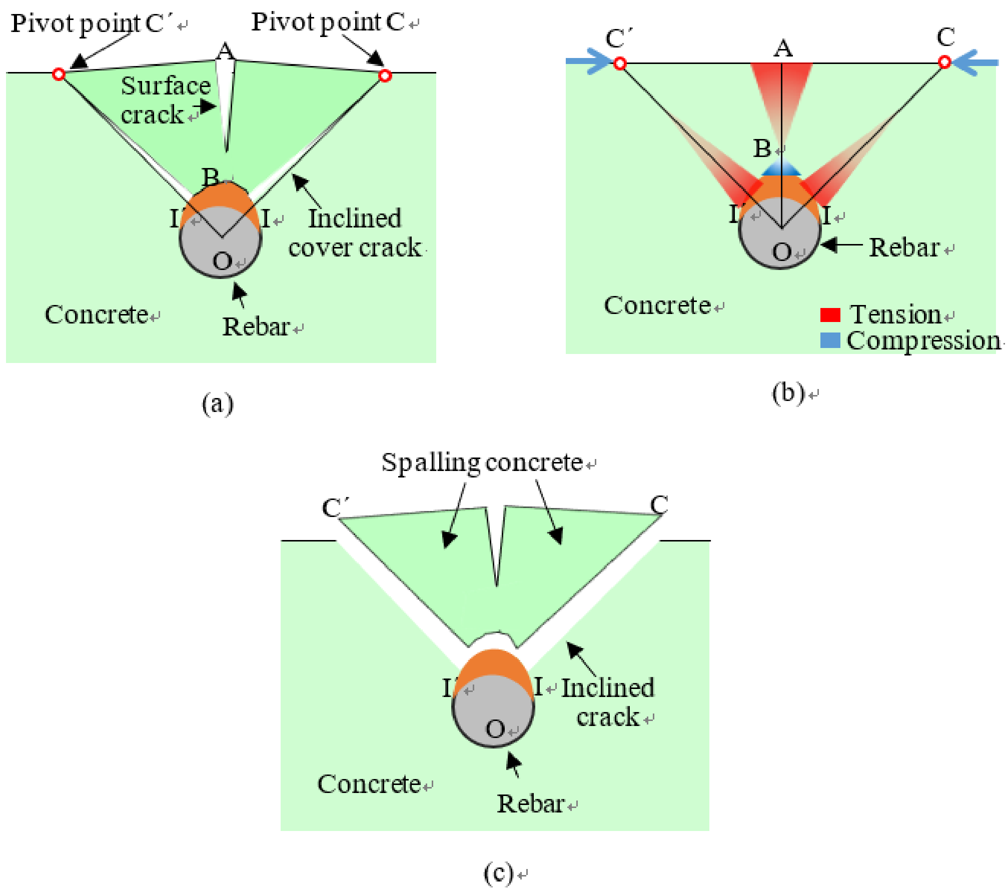

Fig. 3 Elastic-body-rotation model of cracking of cover due to rebar corrosion (a) concrete rotation and cracks, (b) stress map of concrete, and (c) cover spalling caused by inclined cracks

For comprehensiveness, the proposed cover cracking model is briefly described here. As shown in Fig. 3a, the pressure from the corrosion-caused expansion pushes against the concrete cover, which causes the concrete bodies ABIC and ABI′C′ to rotate about the pivot points, C and C′. Such movement results in tensile stress concentration at Points A, I and I′ and concentrated compressive stresses at Points B, C and C′, as shown in Fig. 3b. Thus, two inclined cracks initiate at Points I and I′ on the cover and spread toward the cover surface along IC and I′C′, respectively, as shown in Fig. 3a. Furthermore, a single crack which is perpendicular to the cover surface starts from Point A and propagates along Line AB toward the rebar as shown in Fig. 3a. This surface crack does not penetrate throughout the entire cover because the concrete near the steel/concrete interface at Point B is in compression. Eventually, when the two inclined cracks along IC and I′C′ reach the cover surface, they cause the concrete cover to spall, as shown in Fig. 3c.

Using the model from [36], the areas of corroded steel that cause the initiation of the inclined cracks and cracks on the concrete cover surface; that is, $V_{\text{steel,Ic}}$ and $V_{\text{steel,Ac}}$, respectively, can be determined by using the following equations:

$$V_{\text{steel,Ic}} = \frac{\pi D}{4(\beta-1)}\left\{\frac{\pi D f_{\text{t}}(D+2c)\sin\varphi}{2E_{\text{c,ef}}[D(1-\cos\varphi)+2c]} + 2d_0\right\} \quad (1)$$

$$V_{\text{steel,Ac}} = \frac{\pi D}{4(\beta-1)}\left\{\frac{f_{\text{t}}(D+2c)^2\tan\varphi^2}{8cE_{\text{c,ef}}} + 2d_0\right\} \quad (2)$$

where D is the diameter of the rebar, β is the ratio of the amount of rust to corroded steel, f_t is the tensile strength of the concrete, c is the cover thickness, φ is the angle of the inclined crack on the concrete cover, d_0 is the thickness of the porous zone, $E_{\text{c,ef}} = E_{\text{c}}/(1+\phi_{\text{ct}})$ is the effective elastic modulus of the concrete, E_c is the elastic modulus of the concrete and ϕ_{ct} is the creep coefficient of the concrete.

The areas of corroded steel V_{steel} can be obtained with the width of the crack mouth opening displacement CMOD_{A} of the cover surface, and bulging at Point A, d_A, by using the following equations, respectively:

$$V_{\text{steel}} = \frac{\pi D}{4(\beta-1)}\left\{\left(\frac{(D+2c)f_{\text{t}}\tan\varphi}{2E_{\text{c,ef}}} + \text{CMOD}_{\text{A}}\right)\frac{(D+2c)\tan\varphi}{4c} + 2d_0\right\} \quad (3)$$

$$V_{\text{steel}} = \frac{\pi D}{4(\beta-1)}(d_{\text{A}} + 2d_0) \quad (4)$$

Furthermore, the width of the inclined cracks on the cover CMOD_{I} can be obtained based on the area of the corroded steel by using:

$$\text{CMOD}_{\text{I}} = \left[\frac{4(\beta-1)V_{\text{steel}}}{\pi D} - 2d_0\right]\frac{D(1-\cos\varphi)+2c}{(D+2c)\sin\varphi} - \frac{\pi D f_{\text{t}}}{2E_{\text{c,ef}}} \quad (5)$$

3. Experimental program

3.1 Materials and specimens

Ordinary Portland cement (Green Island Cement, Hong Kong) with a strength class of 52.5 N which complies with BS EN 197-1:2011 [50] was used in the experiment. For the fine and coarse aggregates, local crushed granite rock was used and the largest diameter of the coarse aggregate is 10 mm. A polycarboxylate-based superplasticizer was added to the concrete to improve the flowability. The proportions of the concrete mix are summarized in Table 1. The casted concrete specimens were cured in air at a temperature of 20±2 °C and relative humidity of 75-85%. On the 28th day after casting, concrete property tests were carried out in accordance with Hong Kong Construction Standard CS1 [51]. The test results are summarized in Table 2.

Table 1 Concrete mix proportions

Target concrete grade	Water (kg/m^3)	Cement (kg/m^3)	*w/c*	Fine aggregate (kg/m^3)	Coarse aggregate (kg/m^3)	Maximum aggregate (mm)	Super plasticizer (g/m^3)
C30	200	279	0.72	1025	838	10	1000

Table 2 Concrete properties

f_{cu} (MPa)	E_c (GPa)	f_t (MPa)
34.1	24.4	2.35

Notes: f_{cu}, denotes compressive strength (cube 150 mm×150 mm×150 mm); E_c is the Young's modulus, and f_t, is the tensile strength of the concrete cylinder (diameter: 150 mm and height: 300 mm).

The rebars used in the accelerated corrosion test were ribbed carbon steel bars with a diameter of 16 mm and length of 50 mm. The mechanical properties of steel rebars (tensile strength of steel rebars at yield f_y, ultimate tensile strength of steel rebars f_u, and Young's modulus of steel rebars E_s) are summarized in Table 3. They were polished with a steel brush and abrasive paper, as well as rinsed with distilled water.

Table 3 Mechanical properties of steel rebars

f_y (MPa)	f_u (MPa)	E_s (GPa)
540	621	196

The geometry and dimensions of the specimens are shown in Fig. 4, in which *D* is the rebar diameter and *c* is the cover thickness. Two concrete specimens with dimensions of 50 mm×240 mm×150 mm were cast, which are labelled as Specimens 1 and 2. The cover thickness of Specimens 1 and 2 is 10 mm and 20 mm respectively.

The casting direction was parallel to the longitudinal direction of the rebar. The bottom surface of the specimens was sealed with epoxy resin to ensure that no saline solution (NaCl solution) penetrated into the concrete and no rust could escape through the bottom surface.

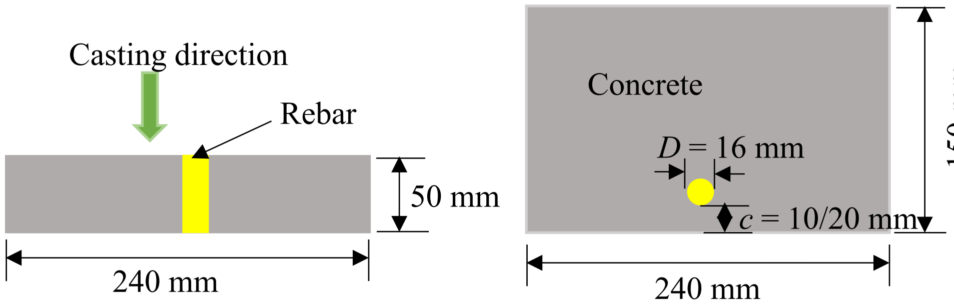

Fig. 4 Geometry and dimensions of specimens

3.2 Accelerated corrosion testing with DIC

Accelerated corrosion tests were conducted by using the DIC technique to measure the surface deformation. The accelerated corrosion technique was used as it is not only faster but also good for controlling the corrosion rate of rebars. Furthermore, the process of concrete cracking would not be significantly affected by the accelerated corrosion test. Therefore, this technique has been widely used to study the effects of rebar corrosion on the deterioration of concrete cover, bond behavior, and residual load-bearing capacity of RC members [15, 47, 52, 53]. Fig. 5 shows the experimental setup. A constant and direct current of 200 μA/cm^2 was applied between the rebar (the anode) and a counter electrode (the cathode) which is made of carbon fiber. About half of the depth of the specimen was immersed into 3.5% NaCl solution. The current and voltage of the specimen were respectively measured with an ammeter and a voltmeter on a daily basis, which were used to calculate the resistance of the specimen with:

$$\mathrm{R} = \frac{V}{I} \tag{6}$$

where R is the resistance of the concrete, V is the voltage and I is the current in the electric circuit.

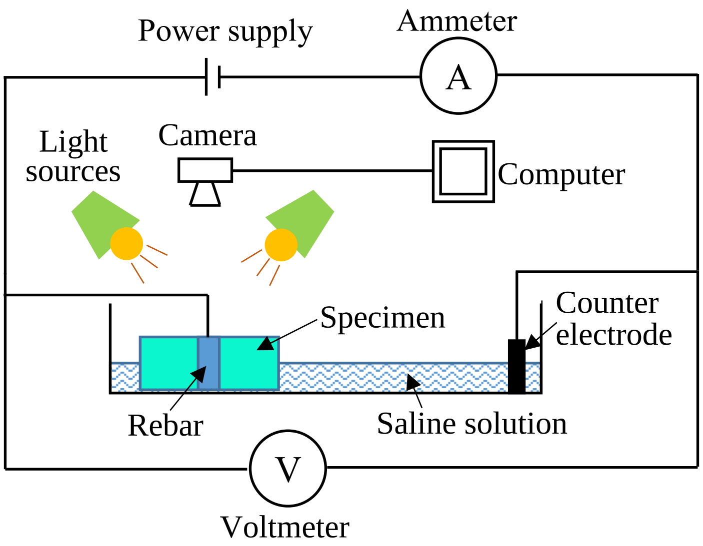

Fig. 5 Experimental setup for accelerated corrosion tests with DIC

Faraday's law of electrolysis was applied to calculate the different levels of corrosion:

$$\Delta m = \frac{ItM}{Fz} \tag{7}$$

where Δm is the theoretical mass loss of the rebar (g), I is the imposed current density (A), t is the corroded time (s), M is the atomic weight of iron (Fe) (55.85 g/mol), F is the Faraday's constant (96,487 C/mol) and z is the ionic charge (2 for iron(II) (Fe^{+2}) and 3 for iron(III) (Fe^{+3})).

DIC was used to capture the full deformation field of the specimen. Random black speckles were sprayed on the surface of the specimens as shown in Fig. 6. Two Canon EOS cameras, 70D and 80D, with a Canon EF-S 18-55 mm IS STM lens were used to take images of Specimens 1 and 2 respectively. The ISO was set at 200 with apertures of f/8 for both cameras. The cameras were placed about 30 cm above the specimens. The focal lengths of the camera lens were set at 55 mm and 35 mm for Specimens 1 and 2 respectively. Generally, each speckle ranges from 3-8 pixels in size to allow for effective correlation. To obtain adequate image contrast, two LED light sources with a direct current were fixed above the specimens. Two reference plates which have similar black speckles as those on the specimens were positioned as shown in Fig. 6. The digital cameras automatically took images every hour during the entire period of testing. The images and reference plates were used to analyze the displacement and strain of the specimens with Optecal, which is a DIC software [54], and previously used in [47, 48].

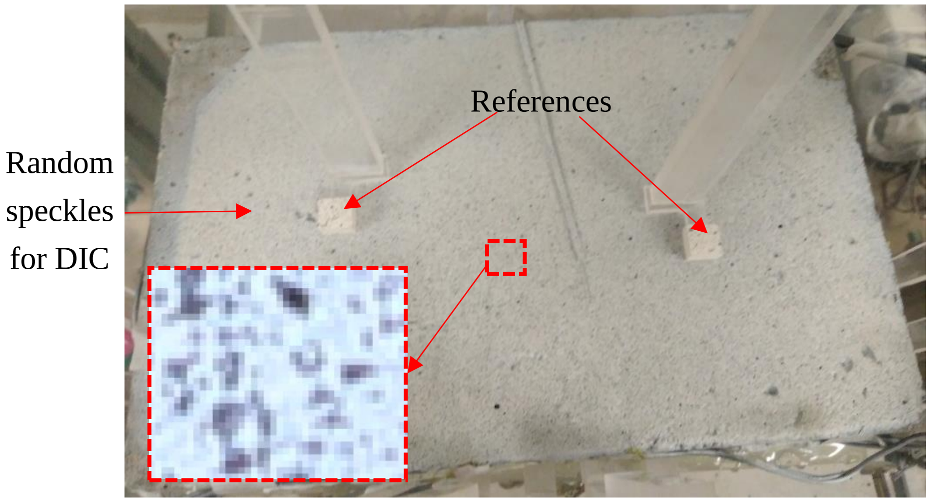

Fig. 6 Specimen with random speckles for DIC

3.3 Layout of strain gauges

Strain gauges were installed onto the surface of the test specimens to measure their strain during testing as illustrated in Fig. 7. Four strain gauges (Nos. 1-1, 1-2, 1-3, and 1-4) with equal distance from the center of the rebar are placed around the rebar in Specimen 1; see Fig. 7(a). Furthermore, five strain gauges (Nos. 1-5, 1-6, 1-7, 1-8, and 1-9) that are spaced 20 mm apart are placed onto the surface of the concrete cover of Specimen 1; see Fig.7(c). Eight strain gauges (Nos. 2-1, 2-2, 2-3, 2-4, 2-5, 2-6, 2-7, and 2-8) are placed around the rebar with two equidistant layers in Specimen 2; see Fig.7(b). Four other strain gauges (Nos. 2-9, 2-10, 2-11, and 2-12) that are spaced 20 mm apart are also placed onto the surface of the concrete cover of Specimen 2; see Fig.7(d). The strain gauge adhesive - PS (polyester and organic peroxide contained) and the coating material - N-1 (chloroprene system rubber) are used to protect the strain gauges from corrosion. On the front of the specimens, strain gauges that are 30 mm length are used, while those that are placed onto the surface of the concrete cover are 10 mm in length. The measurements of the strain gauges were automatically recorded and saved every half an hour with a data logger and a computer.

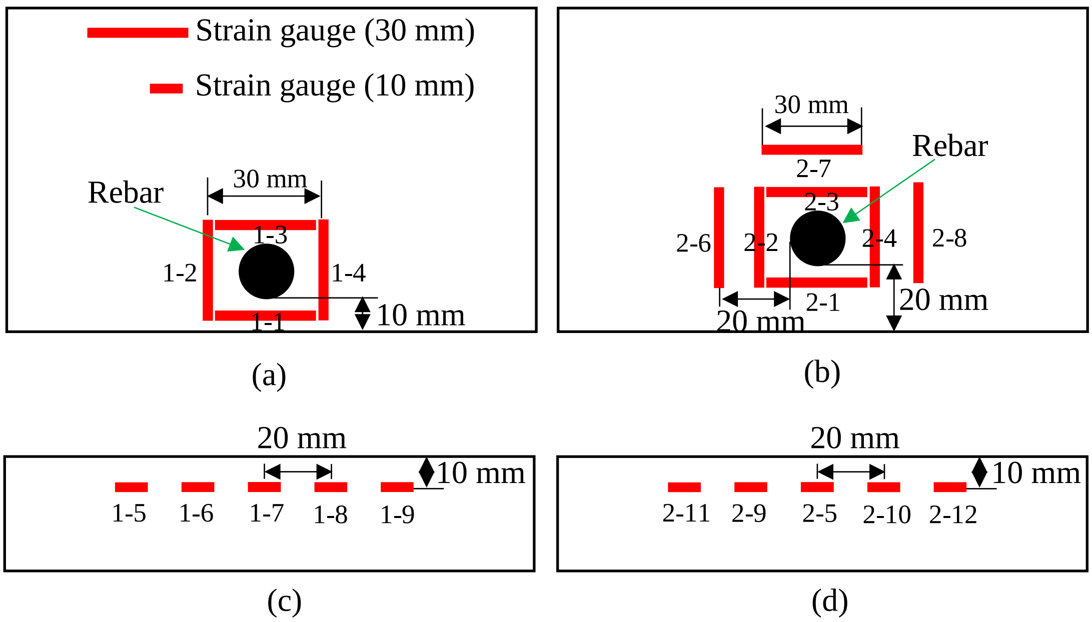

Fig. 7 Layout of strain gauges (a) front view of Specimen 1, (b) front view of Specimen 2, (c) cover surface of Specimen 1, and (d) cover surface of Specimen 2

4. Results and discussion

4.1 Failure mode and map of cracking

All of the corrosion-caused cracks are divided into three categories in this study based on their location and inclined angles, which include: cracks on the surface of the covers, internal cracks, and inclined cracks on the concrete cover as shown in Fig. 8. The cracks on the surface of the cover are found at the thinnest part of the cover and almost perpendicular to the cover surface. The internal cracks are found in the concrete core, which can be but not absolutely vertical to the cover surface. Finally, the inclined cracks are cracks on the cover but form a sharp/obtuse angle to the cover surface.

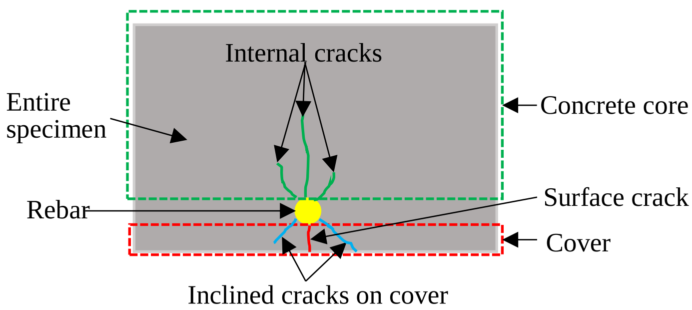

Fig. 8 Three categories of cracks

The COD profiles of the corroded specimens were measured by using an optical microscope with the accuracy of 0.1 mm after the accelerated corrosion test. The failure modes and maps of cracking are presented in Fig. 9 for Specimen 1 after 84 days of corrosion and Fig. 10 for Specimen 2 after 76 days of corrosion. The crack patterns obtained by DIC are shown in Figs. 9a and 10a respectively.

For Specimen 1, the maximum COD is between 0.4 mm - 0.7 mm on the concrete cover as shown in Fig. 9b. It can be seen that the crack inside the concrete cover near the rebar is more narrow than those near the surface of the concrete cover, which means that the COD of the surface crack is reduced from the surface of the cover to the steel/concrete interface [36]. There is an internal crack in the concrete core with a length of 94 mm and 68 mm at the front and back of the specimen respectively; see Figs. 9a and 9c, which means that the expansion of rust not only causes cracks on the concrete cover surface, but also facilitates internal cracks inside the concrete core. Practicing engineers should heed these internal cracks as they cannot be normally detected through a visual inspection, but could affect the integrity and safety of structures. It was observed that the COD of the internal crack in this study shows a trend of decrease from the steel/concrete interface to a region away from the rebar. Furthermore, two inclined cracks on the cover were found on the back of the specimen and the inclined angles are 58.6° and 49° respectively as shown in Fig. 9c. The COD of the two inclined cracks on the cover near the rebar (COD of 0.15 mm) is greater than that near the cover surface (COD of 0.1 mm), which means that the COD is reducing with distance away from the steel/concrete interface towards the cover surface.

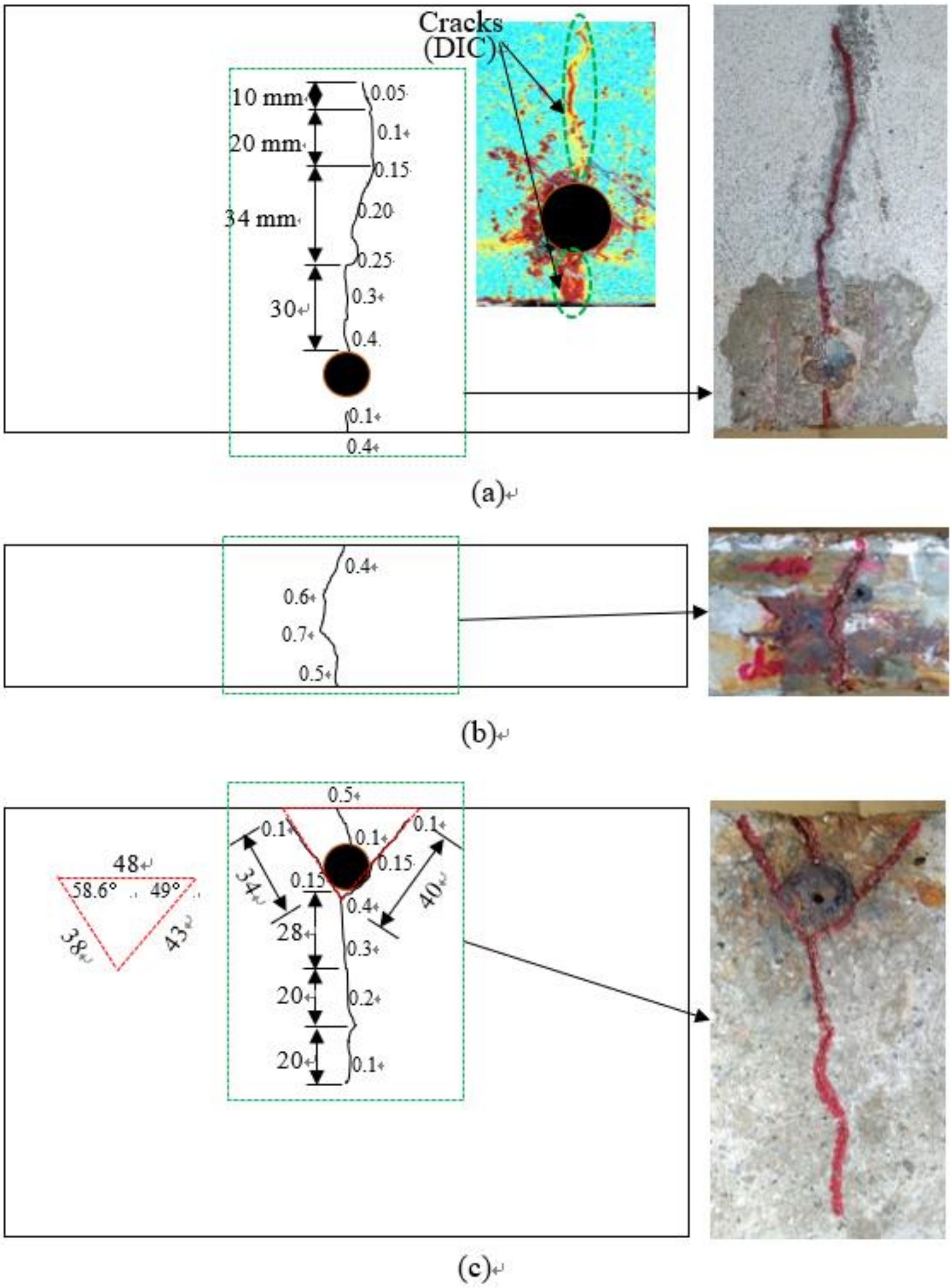

Fig. 9 Failure mode and crack pattern of Specimen 1

(a) front of specimen, (b) cover surface, and (c) back of specimen

The results for Specimen 2 are similar to those observed in Specimen 1; see Fig. 10. The COD profile of the surface crack is decreasing from the cover surface to the steel/concrete interface, while that of the internal and inclined cracks on the cover both decrease with increased distance from the rebar surface. Furthermore, the angles of the inclined cracks are 43°and 32.2° at the front and back of the specimen respectively.

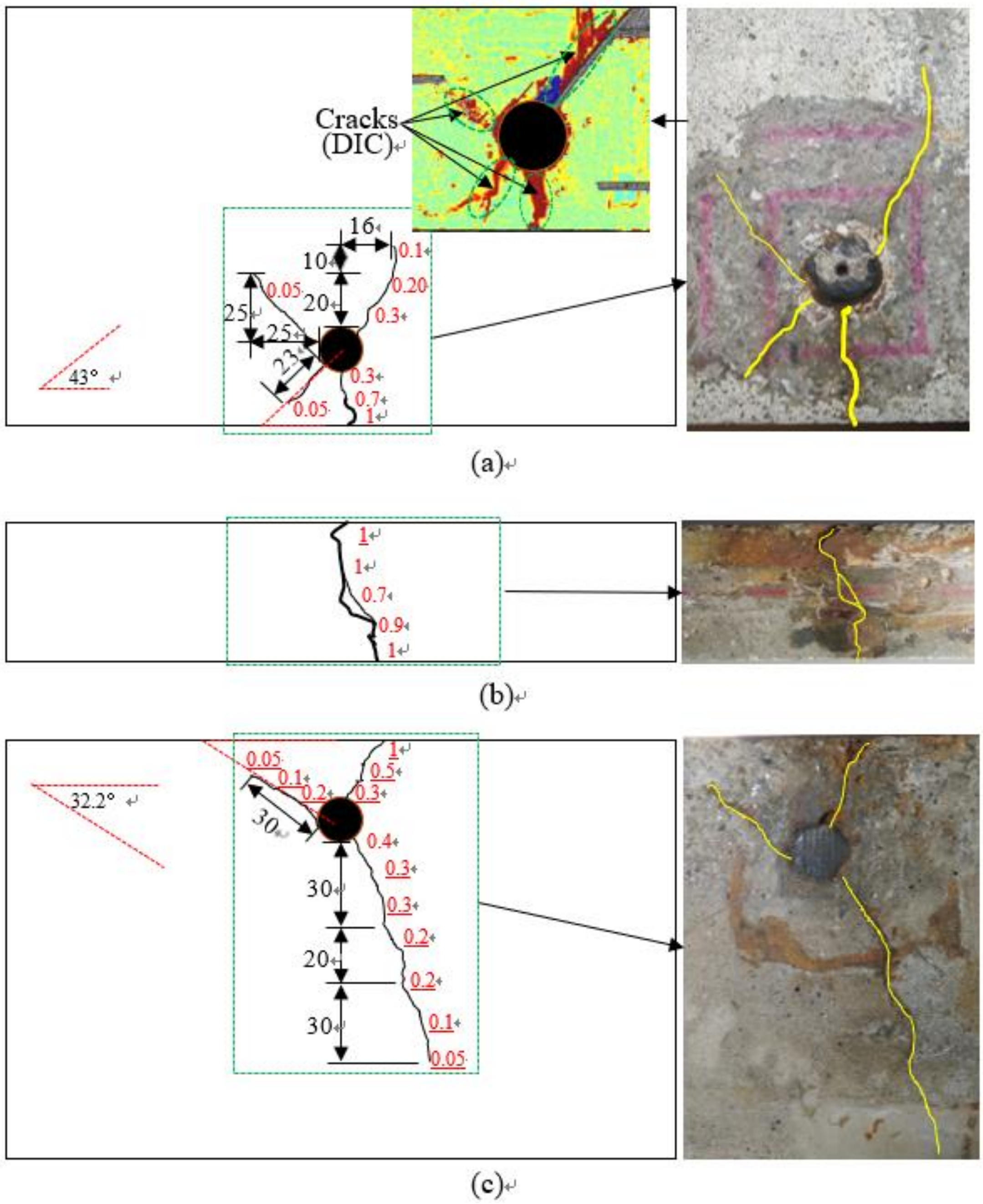

Fig. 10 Failure mode of Specimen 2 and crack pattern

(a) front of specimen, (b) cover surface, and (c) back of specimen

4.2 Failure process

The failure process of Specimen 2 based on the DIC is presented in Fig. 11. Figs. 11a, 11c, 11e and 11g on the left and Figs. 11b, 11d, 11f and h on the right show the rotation and strain distribution of the specimen, respectively. After 5 days of accelerating corrosion, the expansion of the rust pushes against the concrete cover, which causes the left and right parts of the cracked region of the specimen to rotate clockwise and anticlockwise respectively as shown in Fig. 11a. This deformation resulted in the almost simultaneous development of two cracks: one is on the cover surface and the other is an inclined crack on the left part of the specimen as shown in Fig. 11b. After that, the surface crack spreads toward the rebar and increases in width with more rotations of the concrete cover. After about 13 days of corrosion, a second inclined crack emerges on the right part of the specimen as shown in Fig. 11d. Then, both the surface crack and the second inclined crack increases in both length and width. On the 24th day, a third inclined crack emerges on the left part of the cover as shown in Fig. 11f. With an increase in the volume of rust, the vertical surface crack and the second and third inclined cracks increase in width and length as shown in Figs. 11g and 11h. However, in comparison to the development of those cracks, the first inclined crack increased at a much slower rate during the entire period of testing. Moreover, the rotations of the concrete cover gradually increase with an increase in corrosion time during the entire cracking process as shown in Figs. 11a, 11c, 11e and 11g. The mechanism of the cover failure obtained in this experimental study is overall in agreement with the analytical model proposed by the authors in [35].

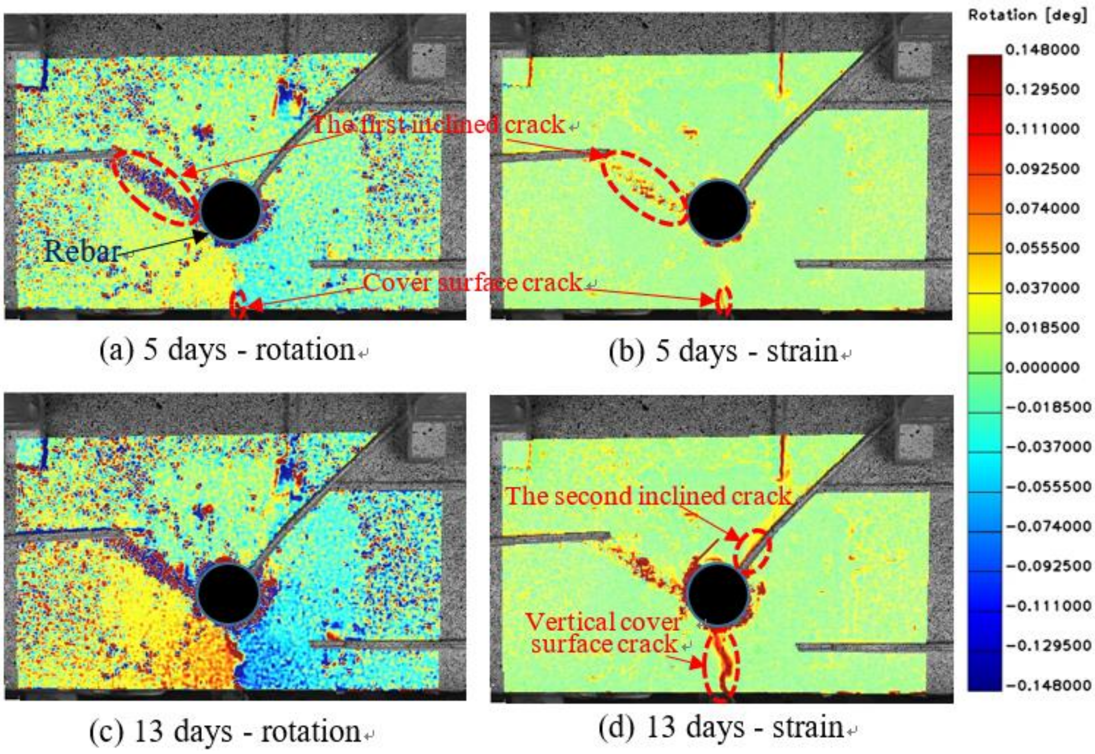

(a) 5 days - rotation (b) 5 days - strain

(c) 13 days - rotation (d) 13 days - strain

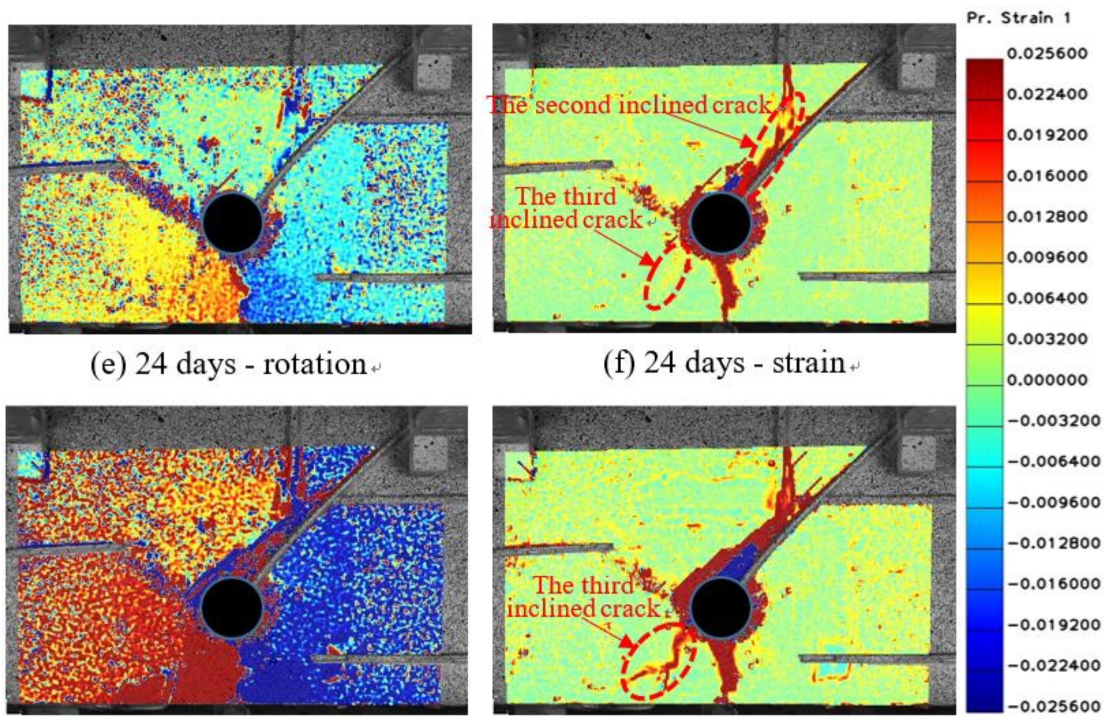

(e) 24 days - rotation (f) 24 days - strain

(g) 76 days - rotation (h) 76 days - strain

Fig. 11 Failure process of Specimen 2

4.3 Corroded rebar

The specimens were manually broken into pieces after carrying out the accelerated corrosion tests. The diameter of the left side of the corroded rebars was measured by using an electronic digital caliper with an accuracy of 0.025 mm. The results are shown in Fig. 12 for the rebar in Specimen 1 (Rebar 1) and Fig. 13 for the rebar in Specimen 2 (Rebar 2). It can be observed that the corrosion of the rebar surface near the cover is more severe than that near the concrete core. This may be due to the fact that after the cracking took place on the surface of the cover, more chloride ions, air and water entered the rebar surface near the cover through the cracks, thus increasing the corrosion rate of steel there. It is also observed that on the rebar surface near the cover, non-uniform corrosion of the steel took place along Rebar 1 as shown in Sections A and B in Fig. 12. It may be caused by partial immersion of the specimen in the saline solution. The degree of saturation and oxygen accessibility along the rebar may not be the same in the sections above and below the solution surface. Compared with Rebar 1, the corrosion along the Rebar 2 is more uniform as shown in Fig. 13.

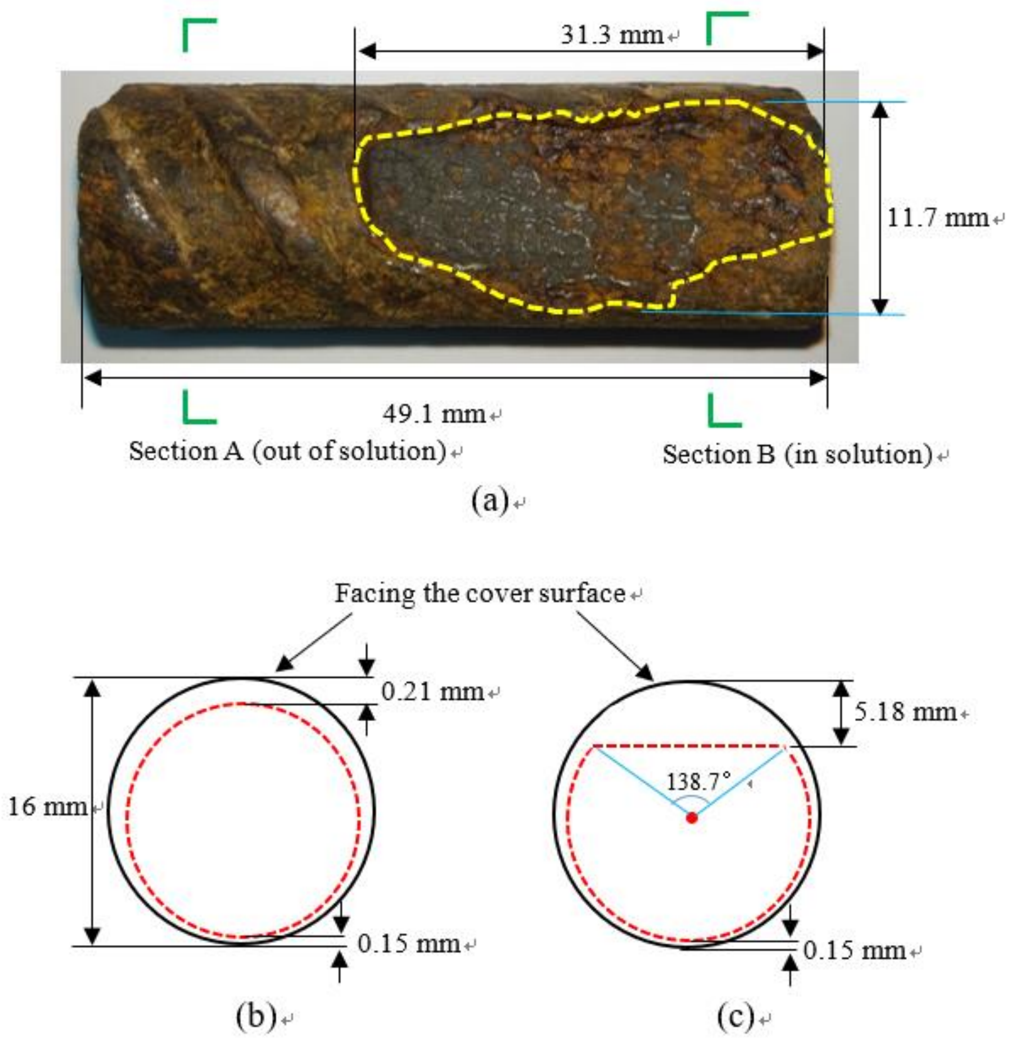

Fig. 12 Corroded rebar in Specimen 1 (Rebar 1): (a) surface, (b) Section A, and (c) Section B

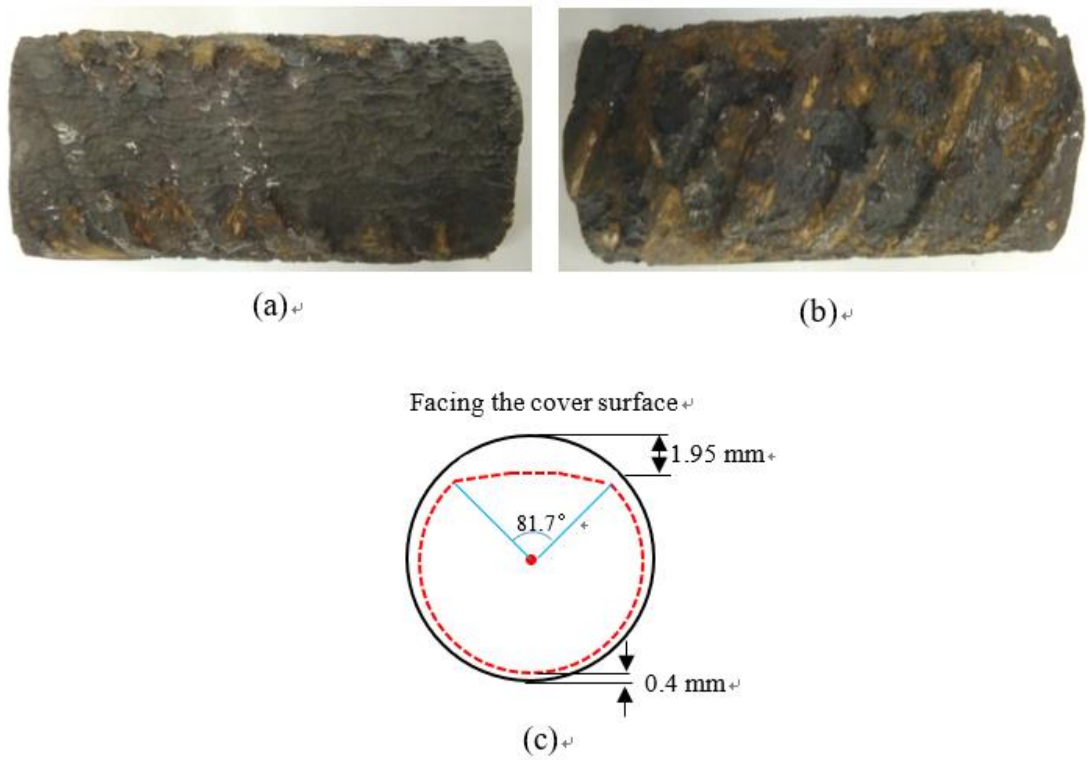

Fig. 13 Corroded rebar in Specimen 2 (Rebar 2): Rebar surface near the cover, (b) Rebar surface near the concrete core, and (c) typical section

The corroded steel rebars were cleaned and their mass loss was weighted in accordance with ASTM G1-03 [55]. The corroded rebars were first cleaned with a light brushing to remove loose and bulky rust, and then immersed in the solution of rust remover. The rebars were kept in the solution for about 5 minutes and then weighted after wiping and drying. This procedure was repeated several times until the weight of corroded rebars was nearly constant.

Table 4 compares the mass loss of the rebars calculated by using Faraday's law on those weighted with an analytical balance (with the accuracy of 0.1 mg). The errors are +1.6% and -2.8% respectively for Rebars 1 and 2. Such small errors means that Faraday's law can be used to calculate the corrosion level of the rebars in accelerated corrosion tests with good accuracy.

Table 4 Comparison of calculated and weighted mass loss of rebars

	Calculated mass loss (g)	Weighted mass loss (g)	Error (%)
Rebar 1	14.660	14.433	+1.6
Rebar 2	10.309	10.609	-2.8

4.4 Displacements at steel/concrete interface

Displacements at eight points of the steel/concrete interface, which were uniformly located around a section of the corroded rebar, were measured by using the

DIC technique after 5, 10, 15 and 20 days of corrosion of the rebar. The results are shown in Fig. 14 in which the displacement ranges of 270°-360° and 0°-90° are displacements at the steel/concrete interface near the cover, and 90°-270° denote the displacement at the rebar surface in the concrete core. It is found that the displacements at the steel/concrete interface are non-uniform. The displacements near the cover are much larger than those on the opposite side, even though the same amount of force from the corrosion-caused expansion is imposed onto both sides of the cover (the force equilibrium around the rebar section). Furthermore, the displacement is the highest at the thinnest part of the cover, i.e. at 0°, which could be attributed to the much lower thickness and confinement capacity of the concrete cover than those of the concrete core, thus causing larger displacements at the steel/concrete interface near the cover.

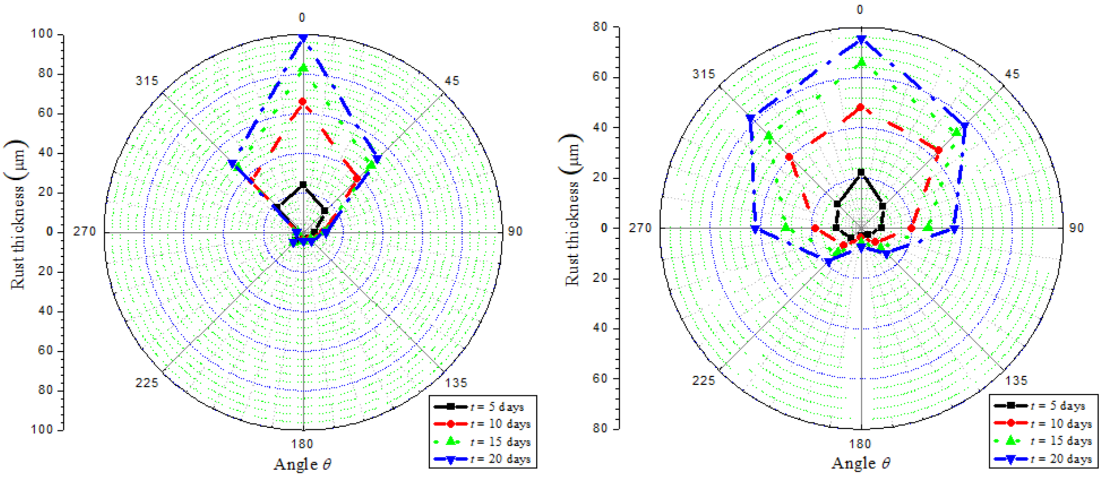

(a) (b)

Fig. 14 Displacements at the steel/concrete interface

(a) Specimen 1 and (b) Specimen 2

4.5 Relationship between amount of total rust and rust that causes cover cracking

There are four sources of rust that make up the total rust, V_{rust}, which include the rust that: (1) fills the initial volume of the corroded steel, V_{steel}; (2) is deposited into the porous zone around the steel/concrete interface, V_{porous}, (3) imposes expansion pressure on the surrounding concrete, V_{net}, and (4) accumulates into or passes out through the corrosion-caused cracks, V_{cracks}. Fig. 15 shows the relationship between V_{rust} and V_{net} in which V_{rust} is obtained by using Faraday's law with Eq. (7) and V_{net} is calculated with the measured displacements at the steel/concrete interface with DIC (as shown in Section 4.4). It can be found that V_{rust} is much higher than V_{net} (Fig. 15a) and the ratio of V_{rust} to V_{net} is between 2.5 and 4 (Fig. 15b). This is because a large volume of rust is deposited into the porous zone (V_{porous}) and cracks (V_{cracks}).

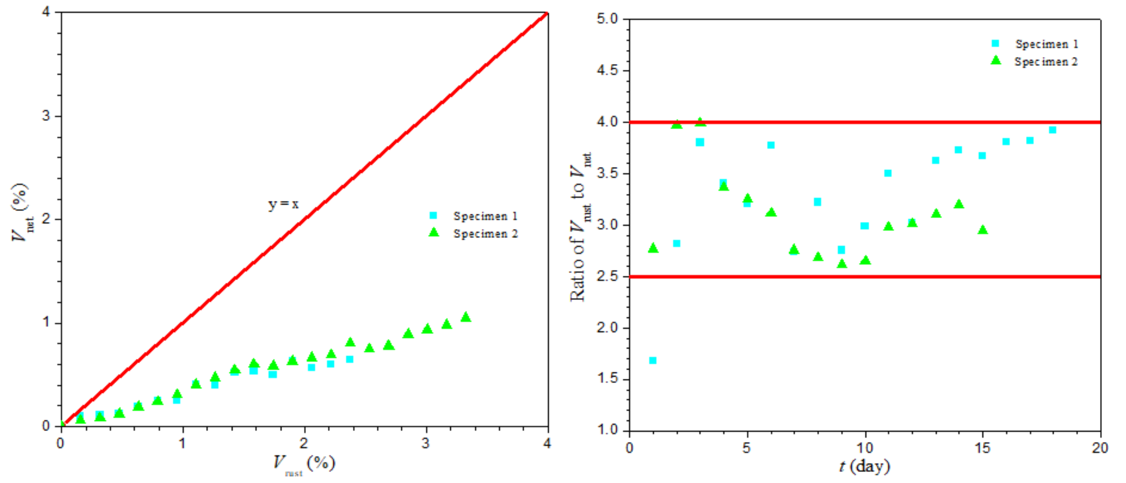

(a) (b)

Fig. 15 Relationship between total rust V_{rust} and rust that causes cover cracking V_{net} (a) comparison of V_{rust} with V_{net} and (b) variation of ratio of V_{rust} to V_{net} with time.

There were two typical reasons causing different cover cracks in the accelerated and natural corrosion situations. The first was that the rust distribution around the rebar is usually uniform in accelerated corrosion tests and non-uniform in natural corrosion [56]. However, in the present accelerated corrosion test, as the thickness of the concrete cover is much thinner than that of the concrete core (see Fig. 4), the cover surface was cracked first, causing more chloride ions, air and water penetrated through the concrete and reached the rebar surface that was in proximity to the concrete cover. As a result, the corrosion of the rebar surface near the cover is more severe than that near the concrete core as shown in Figs. 12-14, which is similar to the natural corrosion [57, 58]. The second reason was due to the differences in corrosion current densities, chemical compositions of rust [56] and the ratio of V_{net}/V_{rust} [59, 60] in accelerated and natural corrosion. These factors could lead to the difference in rust volume V_{net} depositing at the steel-concrete interface even with the same total rust volume V_{rust}, and hence different strain response and crack widths in accelerated corrosion tests. However, in this study, V_{net} is calculated by using the measured displacements around the steel-concrete interface with DIC, which means V_{net} can be obtained directly without the influence of the chemical compositions of rust, the ratio of V_{net}/V_{rust}, and the mechanical properties of rust. Hence the cover cracking process revealed from the accelerated corrosion test together with DIC in this paper should be very similar to that from the natural corrosion.

4.6 Strains

The strains of the two specimens, which were measured with strain gauges, are shown in Figs. 16 and 17 respectively. For Specimen 1, the tensile strain at the cover surface (region of No. 1-7 strain gauge) is much higher than those in the regions of the Nos. 1-1 – 1-4 strain gauges which are closer to the rebar. This is because the rust expanded and pushed against the cover, thus causing the left and the right sides of the cover to rotate clockwise and anticlockwise, respectively [36]. This deformation would result in cracks on the surface of the cover. Among the strains in the regions of the Nos. 1-1 – 1-4 strain gauges which are placed at equal distance from the rebar center, they show an almost equal tensile strain in the first 2 days, but then the strain in the area of No.1-1 increases faster than the others and eventually has the highest strain reading. This is because the cover in the area of No. 1-1 is the least thick and therefore, the most fragile. On the contrary, the concrete core in the area of No. 1-3 is the most thick, and therefore has the lowest strain reading before the cover cracked. The strain in the area of No. 1-7 is also compared with those in the areas of Nos. 1-5, 1-6, 1-8 and 1-9 in Fig. 16b. The concrete in the area of No. 1-7 is always under tension while the concrete in the areas of Nos. 1-5, 1-6, 1-8 and 1-9 is under tension first but later is under compression. The reason for why the concrete in the areas of Nos. 1-5, 1-6, 1-8 and 1-9 could be under compression is due to the continuous rotation of the cracked concrete cover [36].

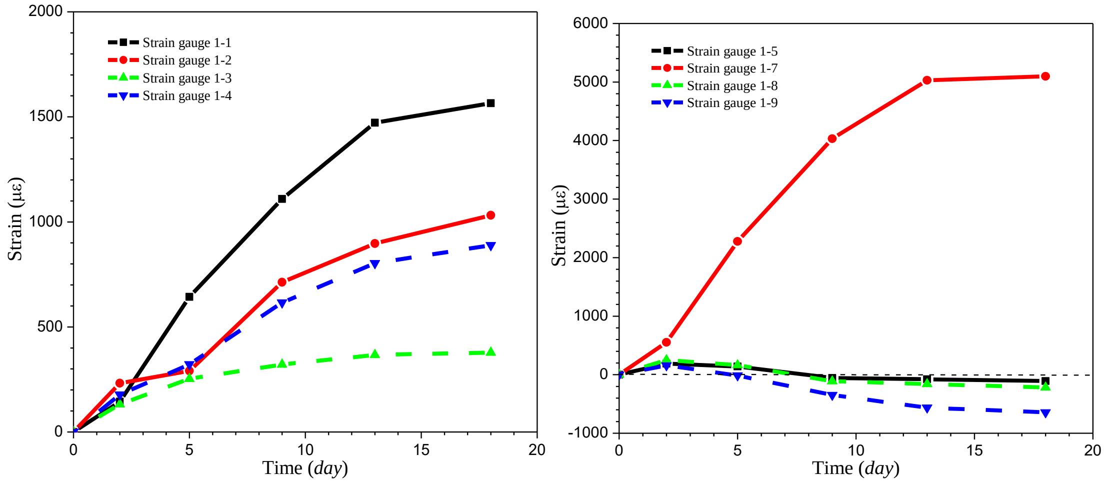

(a) (b)

Fig. 16 Comparison of strain readings in Specimen 1: (a) strains near the rebar and (b) strains on the cover surface

Among the strain readings in the areas with equal distance from the rebar center of Specimen 2; that is, Nos. 2-1 – 2-4 and Nos. 2-5 – 2-8, it can be observed that the ones near the cover surface (Nos. 2-1 and 2-5) are generally the highest as shown in Figs. 17a and 17b. Among the strains in the areas of Nos. 2-1 – 2-4, the strain in the area of No. 2-3 is the lowest at first but later rapidly increases and provides the second highest reading, which is because the cracking of the cover caused a reduction in its resistance capacity. Therefore, the concrete in the area of No. 2-3 had to counter the higher force from the expansion, which caused the cracking of the concrete core.

Furthermore, the strain on the cover surface (No. 2-5) is higher than that in the area of No. 2-1 as shown in Fig. 17c, which is also the case for Specimen 1.

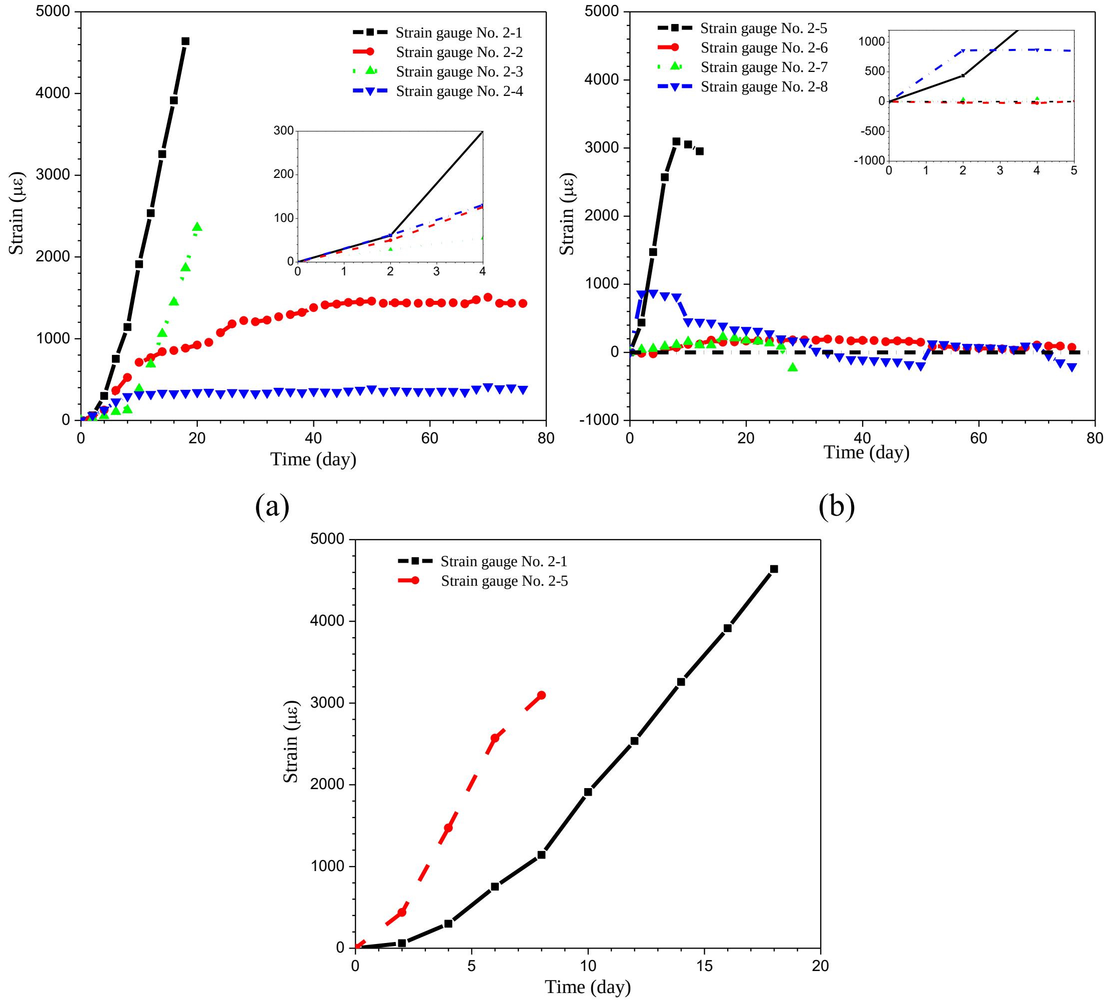

Fig. 17 Comparison of strain in the areas:
(a) Nos. 2-1 – 2-4, (b) Nos. 2-5 – 2-8, and (c) No. 2-5 vs. No. 2-1

4.7 Relationship between maximum expansion thickness of rust and maximum bulging of cover surface

The maximum expansion thickness of rust, $d_{f,max}$, is defined as the expansion displacement at the position of the steel/concrete interface in the least thick part of the cover, i.e. at 0° in Section 4.4. Furthermore, the largest amount of bulging on the surface of the concrete cover, d_A, is found at the position that is vertical to the rebar center. $d_{f,max}$ and d_A were measured by using the DIC technique and their relationships are shown in Fig. 18. It can be observed that $d_{f,max}$ is almost equal to d_A in both specimens.

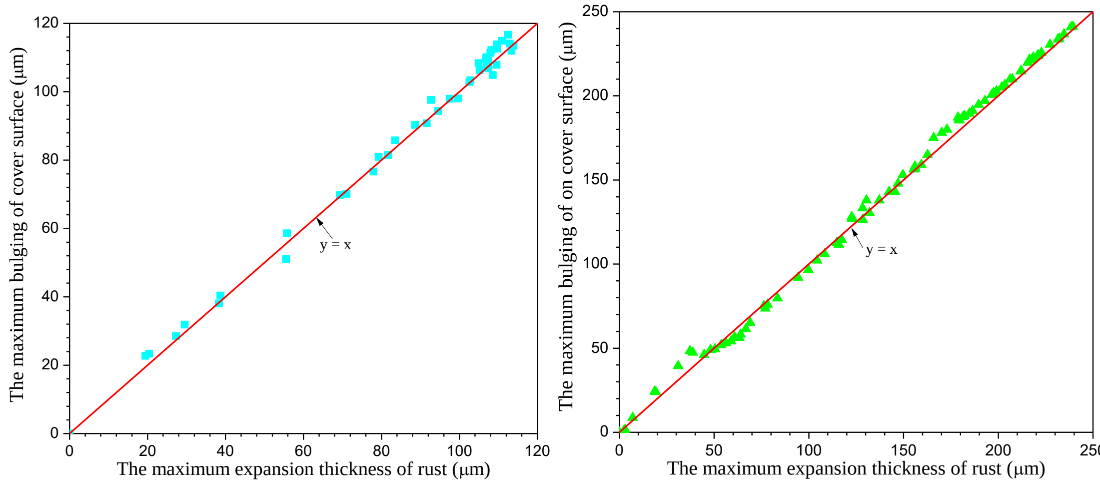

(a) (b)

Fig. 18 Comparison of maximum expansion thickness of rust and largest amount of bulging on surface of concrete cover in (a) Specimen 1 and (b) Specimen 2

4.8 Bulging on surface of concrete cover

Fig. 19 shows a comparison of the bulging on the surface of the concrete cover of Specimen 2 obtained by using the DIC method versus that by using the analytical model developed by the authors in [36], in which the position on the cover surface that is vertical to the rebar center is the initiation point of the bulging. The average of the inclined crack angles on the front and back of Specimen 2, i.e. inclined angle = (43° + 32.2°)/2 = 37.6°, is adopted in the analytical model. It can be found that the shape of the bulge and deformation of the cover surface obtained by using the DIC are generally consistent with those obtained from the analytical model. Furthermore, the bulging at the initiation point is the largest and the bulging almost linearly decreases along the cover surface with an increase in the distance away from the initiation point. The measured profile of the bulging of the cracked cover is a triangular shape which is also consistent with the shape when the profile is determined by using a laser displacement meter [61].

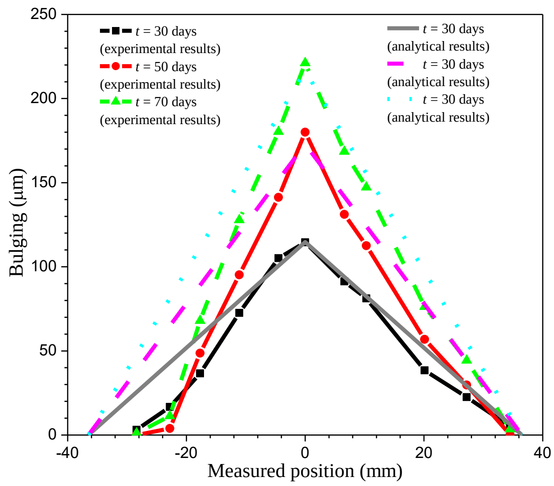

Fig. 19. Comparison of bulging on cover surface obtained from DIC and analytical models [34]

4.9 COD profile of surface cracks

The COD profiles of the surface cracks are measured by using the DIC technique as shown in Fig. 20. It can be observed that the COD profiles at the cover surface are the largest and gradually decrease from the cover surface to the rebar/concrete interface.

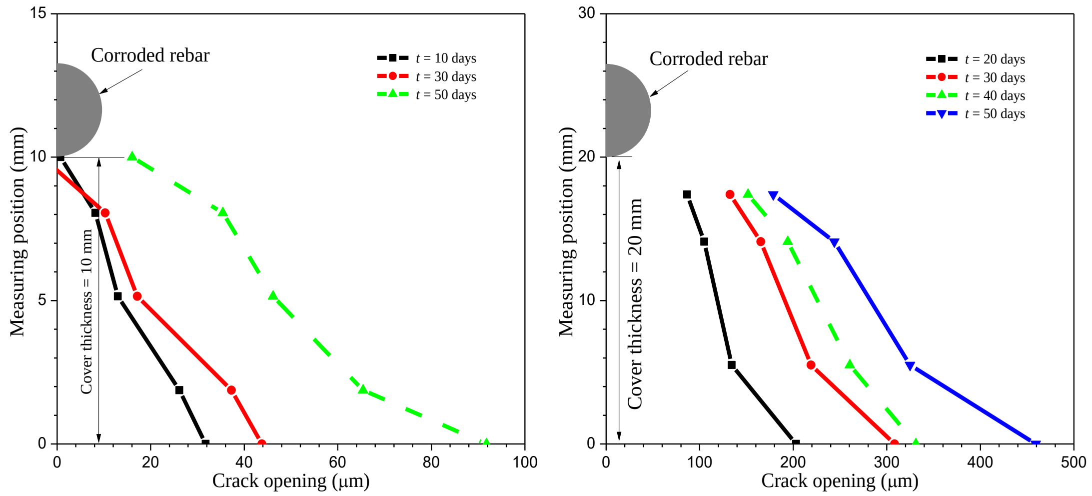

(a) (b)

Fig. 20. COD profiles of the cover of: (a) Specimen 1 and (b) Specimen 2

Fig. 21 is a comparison of the relationship between the maximum expansion thickness of rust and the COD profile at the cover surface obtained by using DIC and the analytical model in [36]. It can be observed that the DIC results are in good agreement with the analytical results.

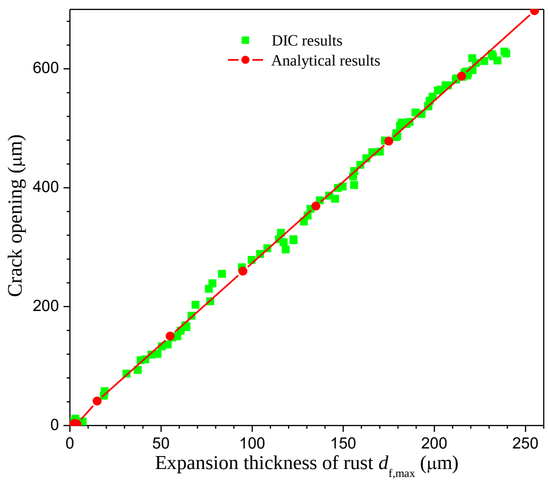

Fig. 21. Relationship between maximum expansion thickness of rust and COD obtained by using DIC and analytical model in [34]

4.10 Electrical resistance of concrete specimens

The electrical resistance of both Specimens 1 and 2 are calculated by using Eq. (6) and their variation with time is shown in Fig. 22. The electrical resistance generally first increases and then gradually decreases. The reason for the increase in resistance might be that the thickness of the rust increases with corrosion time, thus inhibiting the transport of electrons. The reason for the subsequent gradual decrease in resistance might be due to the fact that after the cover cracks, the electrons can still easily migrate through the cracks.

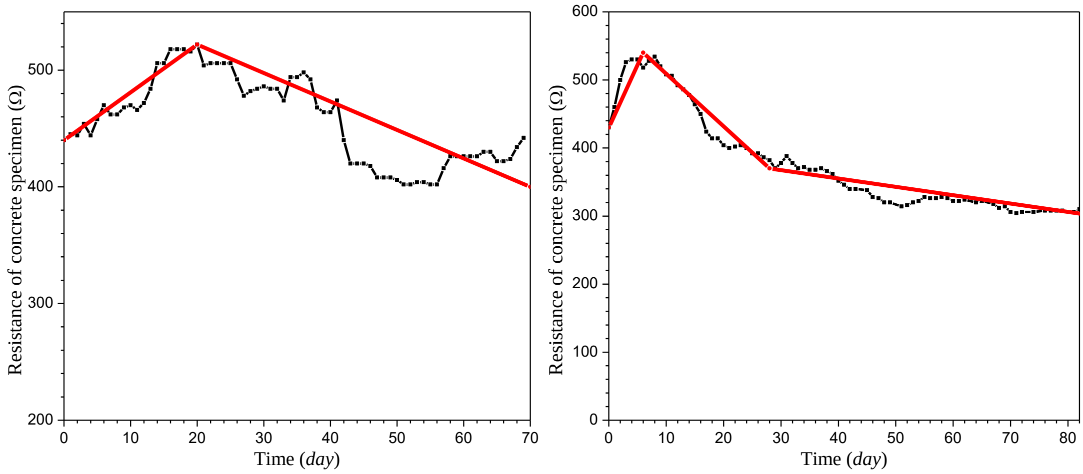

(a) (b)

Fig. 22 Variation in electrical resistance: (a) Specimen 1 and (b) Specimen 2

5. Conclusions

In this study, the failure process of corrosion-caused cover cracking is experimentally investigated by conducting an accelerated corrosion test with the DIC technique. The strain, current and voltage of the specimens are measured with strain gauges, an ammeter and a voltmeter respectively. The following conclusions are drawn from this study:

(1) The failure mode and a map of cracking of the specimens are presented. The COD profile of the surface crack decreases from the cover surface to the steel/concrete interface, while that of the internal and inclined cracks on the cover both decrease with increased distance from the rebar surface. The COD profile of surface crack is also quantitatively analyzed with DIC. Furthermore, two cracks with inclined angles between 30° and 60° are found in the area of the cover.

(2) The failure processes of the specimens are captured by using DIC. The crack propagation on the concrete cover, as well as the deformation and rotation of the cover have been recorded.

(3) The corrosion of the surface of the rebar near the concrete cover is more severe than that in the concrete core in the accelerated corrosion tests.
(4) The displacements at the steel/concrete interface are measured with the DIC technique. It is found that the displacements near the cover are much larger than those in the concrete core. Moreover, the bulging is the highest on the least thick part of the concrete.
(5) The total amount of rust is found to be about 2.5 to 4 times that of the rust that exerts an expansion pressure onto the surrounding concrete. A substantial amount of rust is deposited into the porous zones and cracks.
(6) The tensile strain at the cover surface is much greater than that found on the regions that are closer to the rebar. Among the strains in areas that are spaced equally but in different directions from the rebar center, they are almost equal at first, but then the strain in the area near the cover surface increases more rapidly than the others and gives the highest strain reading.
(7) The DIC results show that the maximum expansion thickness of rust is almost equal to the greatest amount of bulging that occurs on the cover surface.
(8) The measured profile of the bulging of the cracked cover is a triangular shape due to the expansion of rust.
(9) The cover failure mechanism, rotation of the cover, bulging on the surface of the concrete cover and COD profile of the surface crack obtained from this experimental study are generally consistent with those presented in the analytical model in [36].

Finally, the aforementioned findings of this study not only lead to a better understanding of the mechanism and process of corrosion-caused cover cracking but also help researchers and engineers to determine COD profiles and develop more accurate models for assessing the service life of RC structures.

Acknowledgements

This research work is not linked to any specific grant from a public, commercial or non-profit funding agency.

References

[1] R.K.L. Su, Y. Zhang, A double-cylinder model incorporating confinement effects for the analysis of corrosion-caused cover cracking in reinforced concrete structures, Corrosion Science 99 (2015) 205-218.
[2] F. Chen, H. Baji, C.-Q. Li, A comparative study on factors affecting time to cover cracking as a service life indicator, Construction and Building Materials 163 (2018)

681-694.

[3] E. Sola, J. Ožbolt, G. Balabanić, Z.M. Mir, Experimental and numerical study of accelerated corrosion of steel reinforcement in concrete: Transport of corrosion products, Cement and Concrete Research 120 (2019) 119-131.

[4] J. Dong, Y. Zhao, K. Wang, W. Jin, Crack propagation and flexural behaviour of RC beams under simultaneous sustained loading and steel corrosion, Construction and Building Materials 151 (2017) 208-219.

[5] A. Dasar, H. Hamada, Y. Sagawa, D. Yamamoto, Deterioration progress and performance reduction of 40-year-old reinforced concrete beams in natural corrosion environments, Construction and Building Materials 149 (2017) 690-704.

[6] D. Li, R. Wei, F. Xing, L. Sui, Y. Zhou, W. Wang, Influence of non-uniform corrosion of steel bars on the seismic behavior of reinforced concrete columns, Construction and Building Materials 167 (2018) 20-32.

[7] B. Sanz, J. Planas, J.M. Sancho, Study of the loss of bond in reinforced concrete specimens with accelerated corrosion by means of push-out tests, Construction and Building Materials 160 (2018) 598-609.

[8] H. Ye, C. Fu, N. Jin, X. Jin, Performance of reinforced concrete beams corroded under sustained service loads: A comparative study of two accelerated corrosion techniques, Construction and Building Materials 162 (2018) 286-297.

[9] G. Malumbela, M. Alexander, P. Moyo, Interaction between corrosion crack width and steel loss in RC beams corroded under load, Cement and Concrete Research 40(9) (2010) 1419-1428.

[10] M. Otieno, H. Beushausen, M. Alexander, Chloride-induced corrosion of steel in cracked concrete—Part II: Corrosion rate prediction models, Cement and Concrete Research 79 (2016) 386-394.

[11] M. Otieno, H. Beushausen, M. Alexander, Chloride-induced corrosion of steel in cracked concrete – Part I: Experimental studies under accelerated and natural marine environments, Cement and Concrete Research 79 (2016) 373-385.

[12] Y. Gao, Y. Zheng, J. Zhang, S. Xu, X. Zhou, Y. Zhang, Time-dependent corrosion process and non-uniform corrosion of reinforcement in RC flexural members in a tidal environment, Construction and Building Materials 213 (2019) 79-90.

[13] Y. Zhang, R.K.L. Su, Concrete cover delamination model for non-uniform corrosion of reinforcements, Construction and Building Materials 223 (2019) 329-340.

[14] Y. Zhang, R.K.L. Su, Corner cracking model for non-uniform corrosion-caused deterioration of concrete covers, Construction and Building Materials 234 (2020).

[15] L. Dai, H. Bian, L. Wang, M. Potier-Ferry, J. Zhang, Prestress loss diagnostics in pretensioned concrete structures with corrosive cracking, Journal of Structural

Engineering 146(3) (2020).
[16] L. Wang, L. Dai, H. Bian, Y. Ma, J. Zhang, Concrete cracking prediction under combined prestress and strand corrosion, Structure and Infrastructure Engineering 15(3) (2019) 285-295.
[17] J. Zhang, X. Ling, Z. Guan, Finite element modeling of concrete cover crack propagation due to non-uniform corrosion of reinforcement, Construction and Building Materials 132 (2017) 487-499.
[18] K.G. Papakonstantinou, M. Shinozuka, Probabilistic model for steel corrosion in reinforced concrete structures of large dimensions considering crack effects, Engineering Structures 57 (2013) 306-326.
[19] S. Muthulingam, B.N. Rao, Non-uniform time-to-corrosion initiation in steel reinforced concrete under chloride environment, Corrosion Science 82 (2014) 304-315.
[20] E. Chen, C.K.Y. Leung, A coupled diffusion-mechanical model with boundary element method to predict concrete cover cracking due to steel corrosion, Corrosion Science 126 (2017) 180-196.
[21] C.M. Hansson, A. Poursaee, A. Laurent, Macrocell and microcell corrosion of steel in ordinary Portland cement and high performance concretes, Cement and Concrete Research 36(11) (2006) 2098-2102.
[22] K.V. Subramaniam, M. Bi, Investigation of steel corrosion in cracked concrete: evaluation of macrocell and microcell rates using Tafel polarization response, Corrosion Science 52(8) (2010) 2725-2735.
[23] R. Zhang, A. Castel, R. François, Concrete cover cracking with reinforcement corrosion of RC beam during chloride-induced corrosion process, Cement and Concrete Research 40(3) (2010) 415-425.
[24] D. Li, R. Wei, L. Li, X. Guan, X. Mi, Pitting corrosion of reinforcing steel bars in chloride contaminated concrete, Construction and Building Materials 199 (2019) 359-368.
[25] Q. Liu, R.K.L. Su, A Wasserstein distance-based analogous method to predict distribution of non-uniform corrosion on reinforcements in concrete, Construction and Building Materials 226 (2019) 965-975.
[26] Y. Liu, R. Weyers, Modeling the time-to-corrosion cracking in chloride contaminated reinforced concrete structures, ACI Materials Journal 95(6) (1998) 675-681.
[27] T. El Maaddawy, K. Soudki, A model for prediction of time from corrosion initiation to corrosion cracking, Cement and Concrete Composites 29(3) (2007) 168-175.
[28] C. Lu, W. Jin, R. Liu, Reinforcement corrosion-induced cover cracking and its

time prediction for reinforced concrete structures, Corrosion Science 53(4) (2011) 1337-1347.
[29] Y. Zhao, J. Yu, W. Jin, Damage analysis and cracking model of reinforced concrete structures with rebar corrosion, Corrosion Science 53(10) (2011) 3388-3397.
[30] X. Zhang, M. Li, L. Tang, S.A. Memon, G. Ma, F. Xing, H. Sun, Corrosion induced stress field and cracking time of reinforced concrete with initial defects: Analytical modeling and experimental investigation, Corrosion Science 120 (2017) 158-170.
[31] B.S. Jang, B.H. Oh, Effects of non-uniform corrosion on the cracking and service life of reinforced concrete structures, Cement and Concrete Research 40(9) (2010) 1441-1450.
[32] Z. Cui, A. Alipour, Concrete cover cracking and service life prediction of reinforced concrete structures in corrosive environments, Construction and Building Materials 159 (2018) 652-671.
[33] S. Guzmán, J.C. Gálvez, Modelling of concrete cover cracking due to non-uniform corrosion of reinforcing steel, Construction and Building Materials 155 (2017) 1063-1071.
[34] S. Caré, Q. Nguyen, K. Beddiar, Y. Berthaud, Times to cracking in reinforced mortar beams subjected to accelerated corrosion tests, Materials and Structures 43(1-2) (2010) 107-124.
[35] C.Q. Li, R.E. Melchers, J.J. Zheng, Analytical model for corrosion-induced crack width in reinforced concrete structures, ACI Structural Journal 103(4) (2006) 479-487.
[36] R.K.L. Su, Y. Zhang, A novel elastic-body-rotation model for concrete cover spalling caused by non-uniform corrosion of reinforcement, Construction and Building Materials 213 (2019) 549-560.
[37] K. Bhargava, A.K. Ghosh, Y. Mori, S. Ramanujam, Modeling of time to corrosion-induced cover cracking in reinforced concrete structures, Cement and Concrete Research 35(11) (2005) 2203-2218.
[38] K. Kim, S. Jang, B. Jang, B. Oh, Modeling mechanical behavior of reinforced concrete due to corrosion of steel bar, ACI Materials Journal 107(2) (2010) 106-113.
[39] K. Vu, M. Stewart, J. Mullard, Corrosion-induced cracking: experimental data and predictive models, ACI Structural Journal 102(5) (2005) 719-726.
[40] D. Qiao, H. Nakamura, Y. Yamamoto, T. Miura, Crack patterns of concrete with a single rebar subjected to non-uniform and localized corrosion, Construction and Building Materials 116 (2016) 366-377.
[41] W. Zhu, R. François, Y. Liu, Propagation of corrosion and corrosion patterns of bars embedded in RC beams stored in chloride environment for various periods,

Construction and Building Materials 145 (2017) 147-156.
[42] B. Pan, K. Qian, H. Xie, A. Asundi, Two-dimensional digital image correlation for in-plane displacement and strain measurement: a review, 2009, p. 062001.
[43] S. Yoneyama, Basic principle of digital image correlation for in-plane displacement and strain measurement, Advanced Composite Materials 25(2) (2016) 105-123.
[44] T.M. Fayyad, J.M. Lees, Experimental investigation of crack propagation and crack branching in lightly reinforced concrete beams using digital image correlation, Engineering Fracture Mechanics 182 (2017) 487-505.
[45] Y. Jiang, Z. Jin, T. Zhao, Y. Chen, F. Chen, Strain Field of Reinforced Concrete under Accelerated Corrosion by Digital Image Correlation Technique, Journal of Advanced Concrete Technology 15(7) (2017) 290-299.
[46] S. Care, Q.T. Nguyen, V.L. L'Hostis, Y. Berthaud, Mechanical properties of the rust layer induced by impressed current method in reinforced mortar, Cement and Concrete Research 38(8-9) (2008) 1079-1091.
[47] Q. Liu, R.K.L. Su, A displacement-based inverse analysis method to estimate in-situ Young's modulus of steel rust in reinforced concrete, Engineering Fracture Mechanics 192 (2018) 114-128.
[48] D.T.W. Looi, R.K.L. Su, B. Cheng, H.H. Tsang, Effects of axial load on seismic performance of reinforced concrete walls with short shear span, Engineering Structures 151 (2017) 312-326.
[49] A. Michel, B.J. Pease, A. Peterová, M.R. Geiker, H. Stang, A.E.A. Thybo, Penetration of corrosion products and corrosion-induced cracking in reinforced cementitious materials: Experimental investigations and numerical simulations, Cement and Concrete Composites 47 (2014) 75-86.
[50] B.S. Institution, Cement. Composition, specifications and conformity criteria for common cements, BSI, 2011.
[51] C.E.a.D.D.o.H. Kong, Construction Standard CS1: Testing Concrete vol. 1, 1990.
[52] M.W.T. Mak, P. Desnerck, J.M. Lees, Corrosion-induced cracking and bond strength in reinforced concrete, Construction and Building Materials 208 (2019) 228-241.
[53] X. Liu, Y. Li, Static bearing capacity of partially corrosion-damaged reinforced concrete structures strengthened with PET FRP composites, Construction and Building Materials 211 (2019) 33-43.
[54] Optecal DIC Software, CV Measurements, Berkeley, CA, 2015.
[55] A. International, G1-03 Standard Practice for Preparing, Cleaning, and Evaluating Corrosion Test Specimens, 2003.
[56] A. Poursaee, C. Hansson, Potential pitfalls in assessing chloride-induced

corrosion of steel in concrete, Cement and Concrete Research 39(5) (2009) 391-400.
[57] Y. Zhao, A.R. Karimi, H.S. Wong, B. Hu, N.R. Buenfeld, W. Jin, Comparison of uniform and non-uniform corrosion induced damage in reinforced concrete based on a Gaussian description of the corrosion layer, Corrosion Science 53(9) (2011) 2803-2814.
[58] C. Fu, N. Jin, H. Ye, J. Liu, X. Jin, Non-uniform corrosion of steel in mortar induced by impressed current method: An experimental and numerical investigation, Construction and Building Materials 183 (2018) 429-438.
[59] T.A. El Maaddawy, K.A. Soudki, Effectiveness of impressed current technique to simulate corrosion of steel reinforcement in concrete, Journal of Materials in Civil Engineering 15(1) (2003) 41-47.
[60] Á. Bazán, E. Reyes, J.C. Gálvez, Influence of pore networking and electric current density on the crack pattern in reinforced concrete test due to pressure rust layer at early ages of an accelerated corrosion test, Materials 12(15) (2019).
[61] K.K. Tran, H. Nakamura, K. Kawamura, M. Kunieda, Analysis of crack propagation due to rebar corrosion using RBSM, Cement and Concrete Composites 33(9) (2011) 906-917.